Received: 30 May 2020 | Revised: 17 November 2020 | Accepted: 14 December 2020

DOI: 10.1002/2050-7038.12774

SPECIAL ISSUE PAPER

WILEY

Modeling, analysis, and design of novel control scheme for two-input bidirectional DC-DC converter for HESS in DC microgrid applications

Srinivas Punna | **Udaya Bhasker Manthati** | **Arunkumar Chirayarukil Raveendran**

Department of Electrical Engineering,
NIT-Warangal, Hanamkonda, India

Correspondence
Srinivas Punna, Department of Electrical Engineering, NIT-Warangal, Hanamkonda, Telangana, India.
Email: srinu240@student.nitw.ac.in

Handling AE: Prof. Mekhilef, Saad

Summary

This paper presents an advanced controller for multi-input bidirectional DC–DC power converter (MIPC) for hybrid energy storage system (HESS). When batteries are used for energy storage, their rates of charge and discharge are low, and this sets up current stress on the battery, decreasing its life. Supercapacitors (SC), with their higher power density, can react immediately to sudden fluctuations and can take care of this issue. However, SC alone cannot be used for storage, as they cannot supply power for longer durations. In HESS, batteries and supercapacitors are used together, as their contrasting characteristic makes them a perfect combination for energy storage. The HESS is interfaced with DC microgrid using MIPC. MIPC provides decoupled control of battery and SC power and also facilitates energy exchange between storage devices within the system. A controller is designed for DC microgrid application, with its operation modified to control both HESS charging and discharging operation, making it a unified controller. Conventional control schemes neglect uncompensated power from the battery system, and power sharing depends entirely on a low-pass filter (LPF). In the control scheme proposed in this paper, uncompensated power from the battery system is utilized to improve the SC system. This approach reduces the current stresses, increases the life cycle of the battery, improves the overall system performance to the step change in PV generation and load demand, and provides faster DC grid voltage regulation. Simulation and experimental results are developed for the proposed controller by varying photovoltaic (PV) generation and load demand, providing faster DC link voltage regulation.

KEYWORDS

battery, DC microgrid, power converter, power quality, supercapacitor

---

List of Symbols and Abbreviations: d_{SC}, Supercapacitor duty cycle; d_B, Battery duty cycle; V_S, Supercapacitor Voltage; V_B, Battery Voltage; i_S, Supercapacitor current; i_B, Battery current; $Gi_{SC}d_{SC}$, Control to SC current transfer function; $Gv_{DC}i_{SC}$, SC current to output voltage of transfer function; Gi_Bd_B, Control to battery current transfer function; RES, Renewable Energy Sources; ESSs, Energy Storage Systems; SC, Supercapacitor; HESS, Hybrid Energy Storage System; EMS, Energy Management Strategy; MIPCs, Multi-Input bidirectional DC-DC Power Converters; AI, Artificial Intelligence; FLC, Fuzzy Logic Control; ANNs, Artificial Neural Networks; GA, Genetic Algorithm; SOC, State of Charge; HEV, Hybrid Electric Vehicle; LPF, Low-Pass Filter; PI, Proportional Integral.

Int Trans Electr Energ Syst. 2021;31:e12774.
https://doi.org/10.1002/2050-7038.12774

1 | INTRODUCTION

In modern electric grid systems, DC microgrid is an attractive technology, providing easy integration with renewable energy sources (RES), energy storage systems (ESS), and electric loads.[1] Among the available RES, solar power generation is the most economical, environment-friendly, and sustainable.

Energy storage systems (ESSs) have very distinct characteristics, and the most commonly used ESS is a battery. However, batteries suffer from slow rate of charge/discharge cycles due to low power density.[2] In recent years, another electrostatic storage component called supercapacitor (SC) is used as an energy storage system. SC are high power density devices that can respond quickly to the fluctuating and transient component of power to maintain stability of the system.[3] The combined action of battery SC is known as hybrid energy storage system (HESS) which improves the system performance and life span of battery.[4-6]

The DC microgrid integration with HESS is an efficient and cost-effective solution. To exploit the advantages of both battery and SC, different configurations of HESS in DC microgrid applications are possible, viz. passive HESS configuration, semi-active HESS configuration, and full-active HESS configuration.[7] In the current approach, full-active configuration with one or more DC/DC converters was utilized for integrating the storage device and DC microgrid.[8] Power conditioning and energy management strategy (EMS) are required parts of a HESS. When DC/DC converters are utilized in HESS, the multi-input bidirectional DC-DC power converters (MIPCs) have better energy exchange performance between input sources compared to multiple single-input bidirectional converters (MSIBC) in full-active parallel configuration. The main advantage of MIPC is fewer components and smaller size. These converters have established additional responsiveness, their circuit topology is simple, unified control of the storage component power flow is bidirectional, they offer high consistency and low production cost and size. The control scheme is used to enhance the voltage regulation while maintaining the proper power flow balance in DC link.[9]

Several control strategies are being utilized for HESS such as artificial intelligence (AI) methods like fuzzy logic control (FLC), artificial neural networks (ANNs), and genetic algorithm (GA).[10] Based on the above control approaches, the SC supports high-frequency power fluctuations and battery supports average or low-frequency power fluctuations.[11]

Several multiple input topologies have been proposed which can interface multiple sources with contrasting characteristics to a common load. In Reference 12, multiple ESSs are interfaced to a three-winding high-frequency transformer wherein each source is connected through a full-bridge circuit. For battery-supercapacitor HESS, eight connected switches are required, and these may affect the overall efficiency as far as dc microgrid application is concerned. An isolated multiport dc-dc converter was presented in References 13,14 which can manage power from multiple energy sources to a common load. But power flow between the sources, if they were replaced by ESSs, was not explored. Even though isolated converters support wide range of voltage levels as well as safety in the form of isolation, energy management of multiple sources is difficult compared to that of nonisolated converters.

A number of multiple input nonisolated dc-dc bidirectional converters for interfacing multiple sources can be found in the literature which offers far more flexibility in implementation and power management than isolated ones.[15-27] In Reference 15, a procedure for developing all possible double-input single-output dc-dc converters was described and was experimentally verified for a system with battery as one input. But, bidirectional power flow between the two input ports was not considered which is necessary for HESS in microgrid applications. A multi-input dc-dc converter for various energy sources of diverse characteristics was proposed in Reference 16, but with no power sharing option between the input sources. Wang et al[17] presented a single inductor–based multiport converter for HESS. The computation and controller effort are much more since the paper uses model predictive control. Moreover, state of charge (SOC)–based analysis is required for the validity of control strategy.

Faraji and Farzanehfard[18] propose a multiport hybrid energy system with PV and battery. The independent use of battery alone will increase the stress on the battery. Also, the proposed converter is not suitable for SC applications. Sato et al[19] also proposed a multiport converter for PV and battery. The proposed circuit was able to integrate battery with PV; however, during various disturbances, the stress on the battery will be high. Yi et al[20] developed unified control of energy management system for PV-battery-based grid for both grid connected and islanded operation. In the proposed control method, battery balances the AC micro grid and DC micro grid power in all different operating conditions. This increases the battery stress, system cost, and reduces the life cycle of the battery. A high-efficiency dual-input interleaved converter was proposed in Reference 25 which is especially suitable for energy storage sources. However, dual-input interleaved converter circuit requires eight switches which makes the control strategy complicated. Few multi-input converters for grid-tied and/or solar applications are reported in References 26-28. Similarly, multi-input converters are also widely used in hybrid electric vehicle (HEV) applications as in References 29-35. However, in all the above multiple input converter topologies, SOC_{SC} is not maintained in predefined limits and protecting SC from over charge and discharge is difficult.

Even though many works about multi-input bidirectional converters are available in literature, little or less importance has been given to their controller development aspects. The main contributions of this work are as follows:

1. A multi-input bidirectional converter-based DC microgrid voltage stabilization is proposed in this paper.
2. Design a unified controller for charging and discharging of battery and SC HESS in order to make DC microgrid stable for load as well as source variations.
3. The proposed control scheme utilizes the battery uncompensated power to improve the performance of overall system.
4. The main advantage of designed two-input bidirectional converter is its energy exchange mode where we can charge SC independently from battery.
5. Improve the DC microgrid voltage regulation, reducing battery stress and increasing lifespan of battery.

A multi-input bidirectional DC-DC converter proposed in Reference 36 is used to interface the HESS to DC microgrid. The converter in Reference 36 has been modified in operation to suit for HESS operation in DC microgrid applications. In conventional control strategy, the total HESS current (charging/discharging) is divided into low-frequency component of current supplied by using battery and high-frequency component of current supplied by using SC, with the help of low-pass filter (LPF). However, in conventional control strategy, battery current tracking error is observed. The error due to slow dynamics of the battery controller and DC-DC converter is not addressed. To address the aforementioned issues, a new proposed control strategy is implemented which provides fast regulation of DC microgrid voltage.[37,38] The proposed control strategy reduces battery stress and increases the lifetime of the battery.

The paper is organized as follows: The detailed investigation of the two-input bidirectional converter is developed in Section 2. Proposed HESS control scheme is depicted in Section 3. Design of proposed controller for HESS is described in Section 4. The simulation results for conventional and proposed schemes are presented in Section 5. The experimental results of the proposed structure are examined in Section 6. The final part of this paper is concluded in Section 7.

2 | HESS SUPPORTED RES CONFIGURATION

In this section, the architecture of two-input bidirectional converter configuration of HESS aided RES is illustrated in Figure 1. Figure 1 includes off-grid RES involving PV and HESS with the arrangement of battery-supercapacitor bank. For DC microgrid, PV generation is one of the most important RES. Boost converter is used to extract maximum power from PV

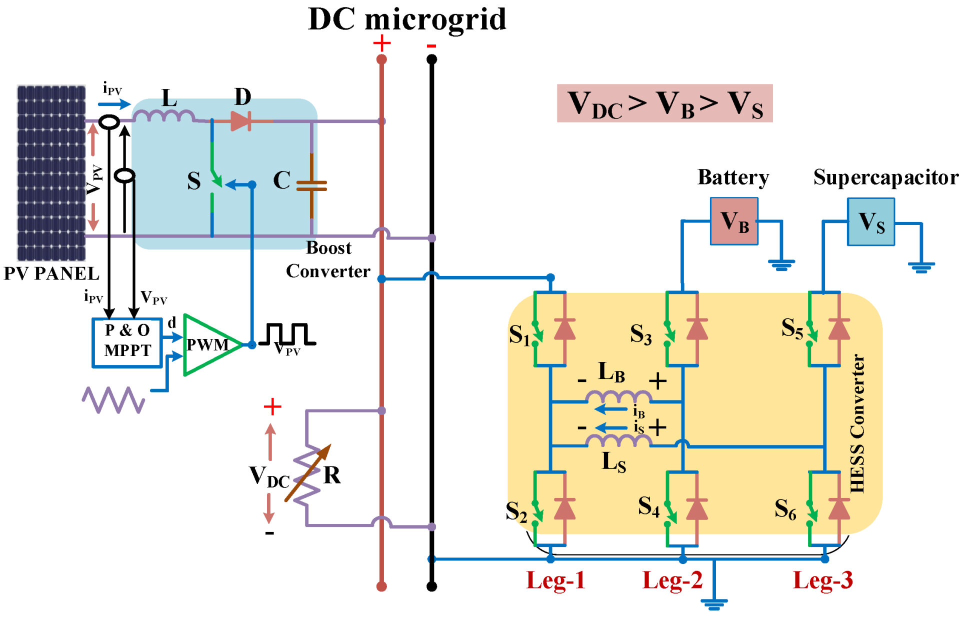

FIGURE 1 DC microgrid architecture operation of HESS with PV system

panel and to interface with the DC microgrid. Combination of battery-SC bank makes the HESS configuration and in case of any mismatch of PV generation and load demand, HESS responds immediately to provide fast regulation of DC grid voltage.

Various modes of operation are presented in detail.[36] Modified converter operation is explained here. It consists of three switching legs. Battery (V_B) and supercapacitor (V_S) modules are connected to legs 2 and 3, respectively. DC microgrid (V_{DC}) is connected to leg 1. In this converter topology, battery voltage is taken as greater than SC voltage and less than DC grid voltage. The high-frequency inductors L_B and L_S are connected between legs 1, 2 and 1, 3, respectively. Different modes of operations are explained in the following sections.

2.1 | Power flow from HESS to DC grid

The switching sequence of the power semiconductor devices in this mode of operation is given in Table 1.The converter operation in this mode can be divided into three time intervals in an overall cycle time of T_S as shown in Figure 2D. The switching devices $S_{5,}$ S_2 are operated with duty cycle d_S and complimentary of these signals drives switches S_6, S_1. Switch S_3 is operated with duty cycle d_B and S_4 is operated with its complementary.

DC microgrid voltage varies from steady-state value whenever there exists a mismatch between PV output power and load power. DC microgrid voltage reduces if PV power generation falls due to reduced solar irradiance or load exceeds PV generation capability. During this mode, HESS supplies deficient power required by the load to balance the

TABLE 1 switching states in different time intervals

Time scale	T_1	T_2	T_3
Operating switches	S_2,S_3,S_5	S_2,S_4,S_5	S_1,S_4,S_6

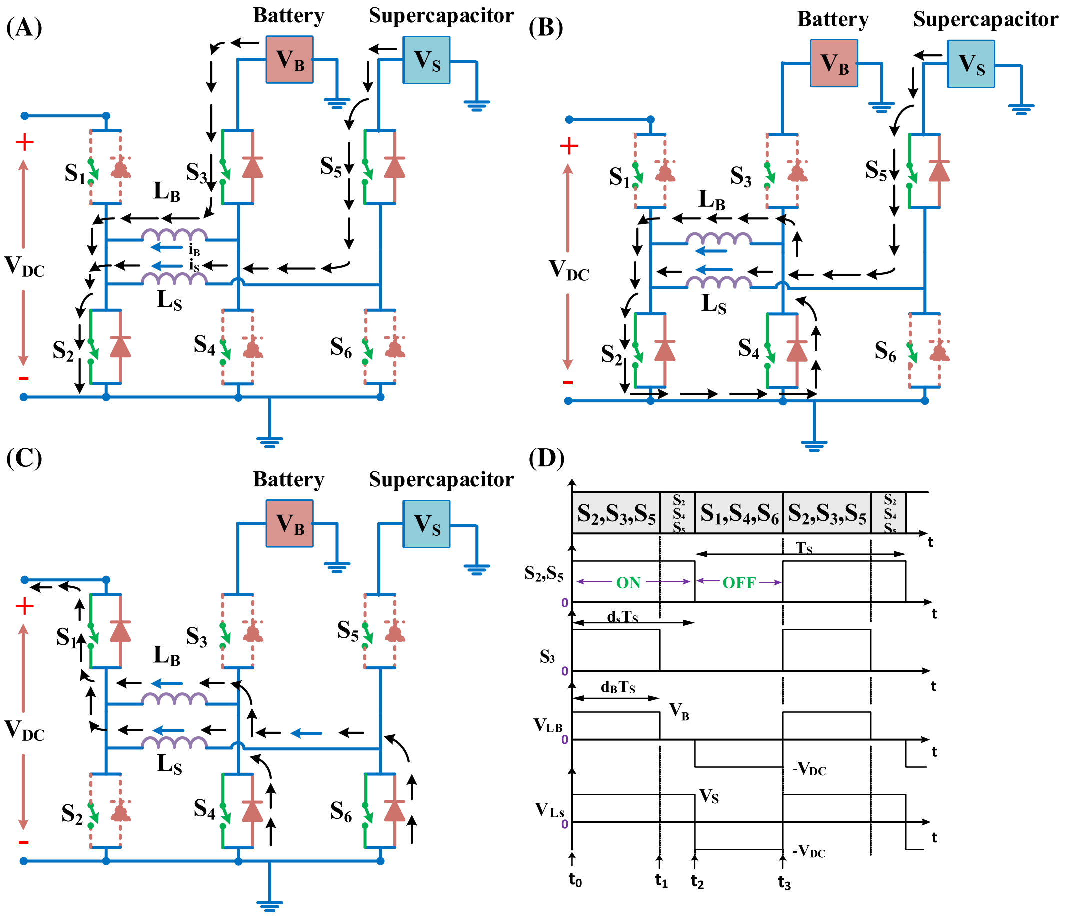

FIGURE 2 Equivalent circuit of two-input bidirectional converter, A, S_2, S_3, S_5 operates, B, S_2, S_4, S_5 operates, C, S_1, S_4, S_6 operates, and D, steady-state waveforms in discharging mode

TABLE 2 switching states in different time intervals.

Time scale	T_1	T_2	T_3
Operating switches	S_1,S_4,S_6	S_2,S_4,S_5	S_2,S_3,S_5

TABLE 3 Relation between different voltages in each mode

Power flow from HESS to DC grid
$V_{DC} = \frac{d_S}{1-d_S}.V_S$, $V_{DC} = \frac{d_B}{1-d_S}.V_B$
Power flow from DC grid to HESS
$V_S = \frac{d_S}{1-d_S}.V_{DC}$, $V_B = \frac{d_S}{1-d_B}.V_{DC}$
Power flow from battery to SC (energy exchange mode)
$V_S = d.V_B$

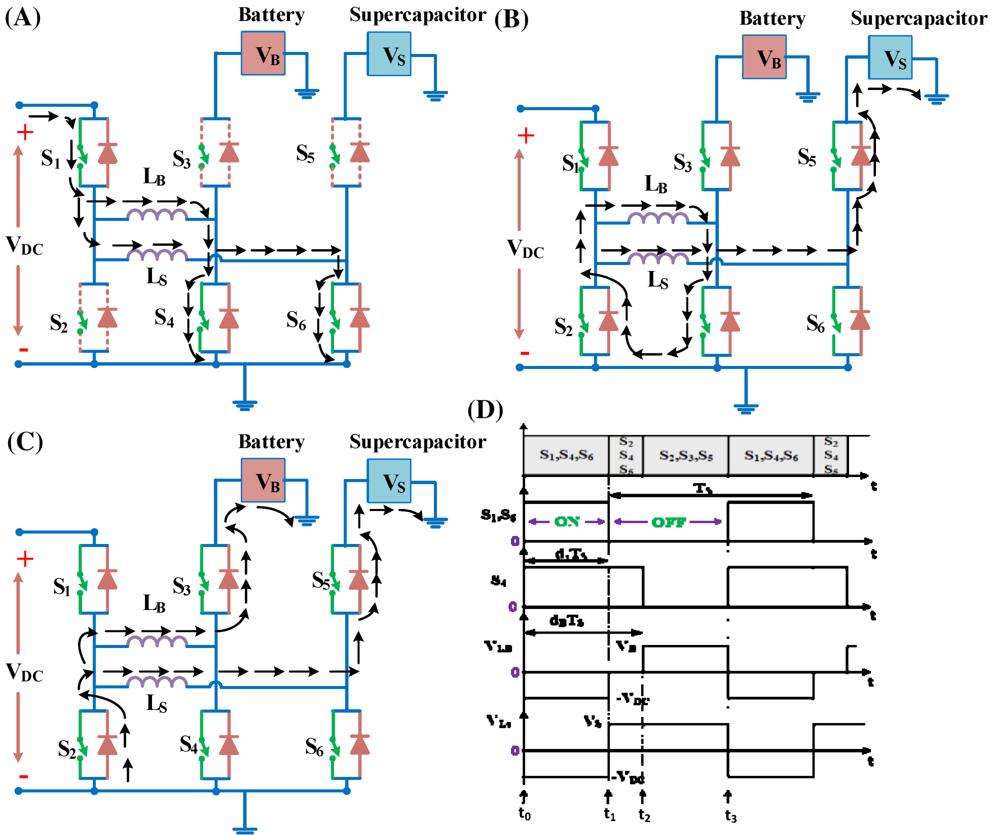

FIGURE 3 Equivalent circuit of two-input bidirectional converter, A, S_1, S_4, S_6 operates, B, S_2, S_4, S_5 operates, C, S_2, S_3, S_5 operates, and D, steady-state waveforms in discharging mode

DC microgrid. By properly controlling the bidirectional converter, power can flow from battery and SC bank to DC microgrid in this mode, equivalent circuit of power flow from HESS to DC microgrid is represented in Figure 2A-C. At time t = t_0, switching devices S_2, S_3, and S_5 are turned on which will increase the inductor currents i_B and i_S linearly with a slopes V_B/L_B and V_S/L_S, respectively. At time t_1, switch S_3 is turned off to provide free-wheeling path for battery current i_B through body diode of S_4. After dead time interval for switches S_3/S_4, the switch S_4 is turned on. At time t_2, the switches S_2 and S_5 are turns off, SC current is to flow through the body diodes of switches S_1 and S_6 with a negative slope of V_{DC}/L_S. Battery current i_B also flows through body diode of S_1 with a negative slope of V_{DC}/L_B. At time t_3, switches S_1, S_4, and S_6 are turned off. Consequently, body diodes of switches S_2, S_3, and S_5 will conduct in order to maintain flow of inductor currents. The currents i_B and i_S flow through with a positive slope of V_B/L_B and V_S/L_S, respectively. After dead time interval, switching pulses are given to switches S_2, S_3, and S_5 turn on with ZVS. Where d_B is the duty ratio of switch S_3, and d_S is the duty ratio of switches S_2 and S_5.

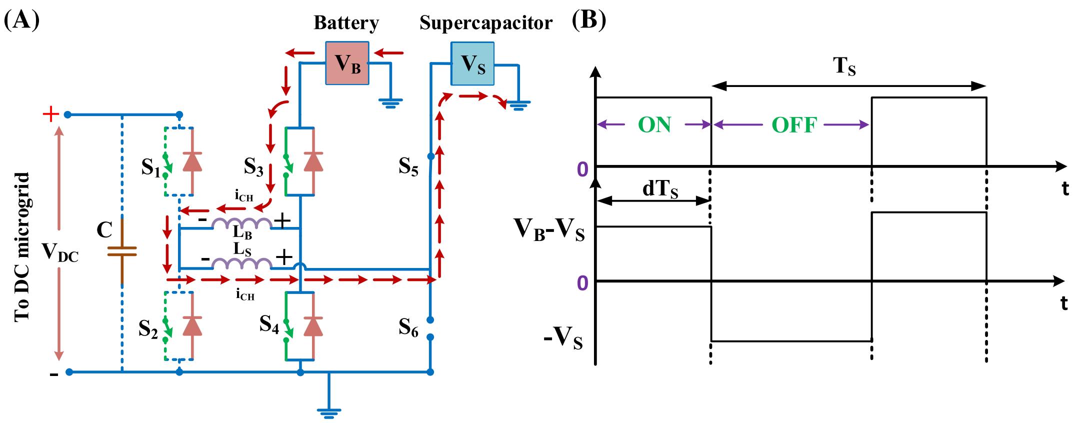

FIGURE 4 HESS energy exchange mode of operation A, equivalent circuit and B, steady-state waveforms

Applying volt-second balance to the voltage across inductors L_B and L_S gives the relation between DC grid voltage to the battery and SC as shown in Table 3.

Since battery voltage V_B is greater than SC voltage V_S, d_B will always be less than d_S. Power flow between battery and SC to DC microgrid can be controlled independently by controlling d_B and d_S.

2.2 | Power flow from DC grid to HESS

Whenever PV-generated power exceeds that required by the load or when load demand decreases, there is excess power existing in the DC microgrid which results in increase of DC grid voltage. The battery and SC will store extra power generated from PV panel. Hence, in this condition, power flows from DC microgrid to HESS. The converter operation using equivalent circuits in this mode can be explained in three switching time intervals as shown in Figure 3A-D. Operating switches in each time interval are tabulated in Table 2.

At time t_0, switches S_1, S_4, and S_6 are operated to increase the inductor currents i_B and i_S with a negative slope of V_{DC}/L_B and V_{DC}/L_S, respectively. In between the time t_0 to t_1, inductors store energy. At time t_1, switches S_1 and S_6 are turned off. Body diodes of S_2 and S_5 are turned on to maintain inductor current i_S. Now, supercapacitor will charge by using energy stored in the inductor L_S. Inductor current i_B free-wheels through body diode of switch S_2. At time instant t_2, switch S_4 is turned off. Inductor current i_S flows through the body diode of switch S_3 with a slope of V_S/L_S. Now, battery gets charged using the energy stored in inductor L_B. At time instant t_3, switches S_2, S_3, and S_5 are turned off, consequently, body diodes of switches S_1, S_4 and S_6 turned on to maintain flow of inductor currents. If d_B is the duty cycle of switch S_4 and d_S is the duty cycle of switches S_1 and S_6, apply volt-second balance to the inductors L_B and L_S gives the relation between SC and battery voltage to DC grid voltage as presented in Table 3.

2.3 | Power flow from battery to SC (Energy exchange mode)

Supercapacitor is a high-power density unit, it cannot deliver power supply for longer duration like battery. To maintain supercapacitor charge within the limits, it has to be charged using battery for proper functioning of HESS. In this mode, power flows from battery to supercapacitor. Equivalent circuit and steady-state waveforms in energy exchange mode operation have been shown in Figure 4.

In energy exchange mode, DC microgrid is disconnected from HESS by opening switches S_1 and S_2. In this mode, switching pairs S_3/S_4 and S_5/S_6 work in complementary manner. Switch S_5 is completely ON in this mode which causes switch S_6 to be completely open circuited as shown in Figure 4. Switch S_3 is operated with duty cycle of d and switch S_5 is completely on to make power flow from battery to supercapacitor like in buck operation. The two inductors are connected in series to reduce the current ripple. By controlling duty cycle d, power flow from battery to supecapacitor can be controlled. Converter switching operation for SC charging/discharging is shown in Figure 5. Applying volt-second

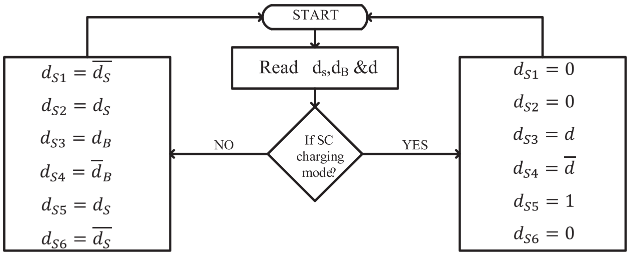

FIGURE 5 Reconfiguration of converter switching operation

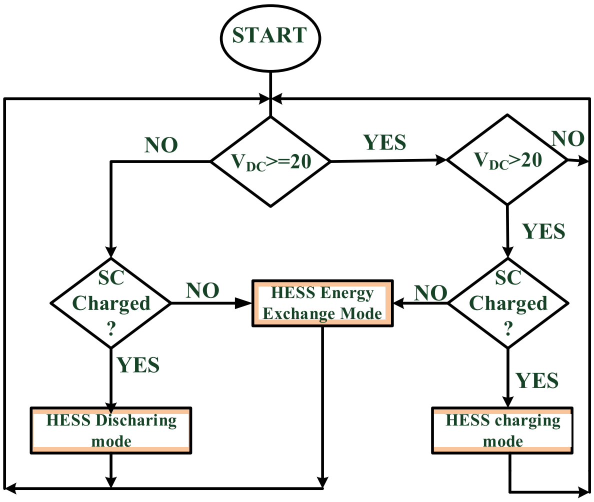

FIGURE 6 Flow chart representation of transition to different modes

balance to equivalent inductance L_{eq} ($L_{eq} = L_B + L_S$) gives the relation between battery voltage and SC voltage as presented in Table 3.

Similarly, power flow from the supercapacitor to battery is also possible by complimentary operation of switch S_3. This operation is similar to the above explanation but indicates boost operation of switch S_4.

2.4 | Mode transitions

The mode of operation is determined from continuous monitoring of supercapacitor SOC and present condition of DC microgrid voltage. Battery energy does not deplete as quickly compared to the supercapacitor, so battery SOC is not considered in this work. Transition of different operational modes is shown in Figure 6. HESS is put into the charging mode, when DC microgrid voltage is more than the set reference voltage, provided supercapacitor SOC is in prescribed limits. When DC microgrid voltage is less than the set reference voltage, HESS is put into the discharge mode provided supercapacitor SOC is in safe limits. If supercapacitor SOC is not maintained in prescribed limits, HESS is put into the energy exchange mode operation, thus isolating the DC microgrid from HESS.

2.4.1 | Mathematical design calculations of filter parameters

For design of the filter inductor for bidirectional DC-DC converter is assumed to be always operated at continuous conduction mode (CCM). The mathematical design of the filter inductor and capacitor for various converters is given in References 39,40.

The calculation of peak-to-peak inductor current ($\triangle i_L$) of boost converter during switch ON period is calculated as

$$\triangle i_L = i_L(DT) - i_L(0)$$

$$\triangle i_L(ON) = \frac{V_{PV}.DT}{L} = \frac{V_{PV}.D}{f_s L} = \frac{V_{DC}.D.(1-D)}{f_s L}. \tag{1}$$

Similarly, $\triangle i_L$ during switch OFF period of time

$$\triangle i_L = i_L(DT) - i_L(T)$$

$$\triangle i_L(OFF) = \frac{(V_{DC}-V_{PV})(1-D)T}{L} = \frac{V_{DC}.D.(1-D)}{f_s L}. \tag{2}$$

In the current experimental work, PV panel source is rated at: MPP voltage (V_{PV}):12 V, MPP current (i_{PV}): 1.34 A and maximum power (P_{max}): 16.08 W. For designing DC microgrid voltage (V_{DC}) to 20 V, load resistance can be selected as follows

$$R_{load} = \frac{{V_{DC}}^2}{P_{max}} = \frac{20^2}{16} = 25\,\Omega.$$

For designing filter inductor, the peak-to-peak inductor current ($\triangle i_L$) is limited to 5% of total current in this work, inductor (L) is defined as follows

$$L = \frac{V_{PV}.D}{f_s.\Delta i_L}. \tag{3}$$

Similarly, the output filter capacitor(C) reduces the voltage ripple, thus can be calculated as

$$C = \frac{D.V_{DC}}{f_s.R_{load}.\Delta V_{DC}}. \tag{4}$$

3 | PROPOSED CONTROL SYSTEM SCHEME OF HESS

The control system block diagram representation of conventional and proposed control scheme is shown in Figure 7A, B. The proposed control scheme will contribute a controller which will not only provide good closed loop performance but also provide stable operation amid converter dynamics and external disturbances. The nominal value of DC link voltage (V_{DC}) is compared with a reference voltage ($V_{DC,ref}$), and the error is offered to the PI controller in both schemes, which generates total current (i_{tot}) from ESS in this process. In the conventional control scheme, total current is divided into low-frequency (I_{LOW}) and high-frequency (I_{HIGH}) components of current using LPF, which is given as reference currents to battery and supercapacitor loops, respectively, and it is represented in Figure 7A. In the conventional control scheme, SC current reference consists of high-frequency component and battery error component which is explained in proposed control scheme. Conventional control scheme neglects battery current error arising due to the battery controller.

The proposed control scheme is represented in Figure 7B. The power flow in DC grid under PV generation, and load changes are classified into two types (a) steady-state power component (P_{std}) and (b) transient power component (P_{tran}). The power balance equation given as

$$P_{dc}(t) - P_{ren}(t) = P_B(t) + P_{SC}(t) = P_{std}(t) + P_{tran}(t), \tag{5}$$

where, $P_{dc}(t)$, $P_{ren}(t)$, $P_B(t)$, and $P_{SC}(t)$ are the DC grid power, RES power, battery, and SC power, respectively. The HESS charges and discharges, maintaining the DC grid voltage in predefined limits. The sum of battery and SC powers are given as

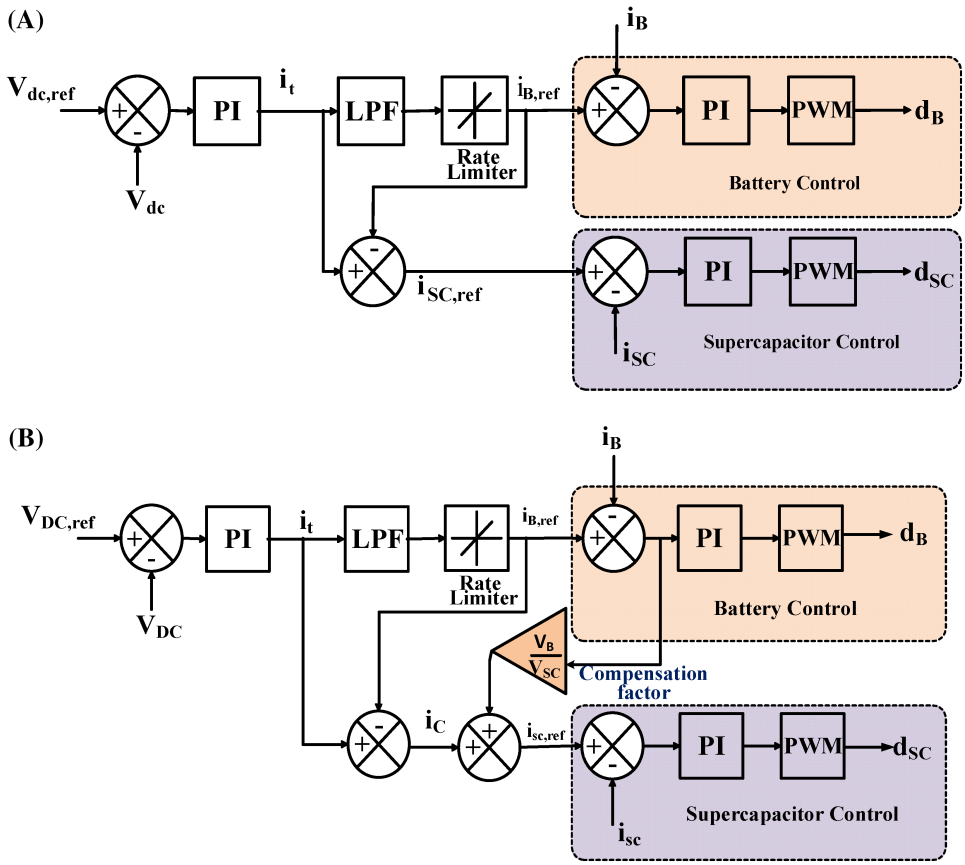

FIGURE 7 Overall control system description for current bifurcation b/w SC and battery unit A, conventional control scheme and B, proposed control scheme

$$P_B(t)+P_{SC}(t)=P_{std}(t)+P_{tran}(t)=V_{DC}.i_{tot}(t). \tag{6}$$

Regulates the DC link voltage by controlling total current demand represented as follows

$$i_{tot}=\frac{P_{std}(t)+P_{tran}(t)}{V_{DC}(t)}=i_{std}(t)+i_{tran}(t). \tag{7}$$

Voltage control loop calculates the total current (i_{tot}) demand as follows:

$$i_{tot}(t)=i_{std}(t)+i_{tran}(t)=K_{p,v}.v_{err}+K_{i,v}.\int v_{err}dt, \tag{8}$$

where $K_{p,v}$ and $K_{i,v}$ are the proportional and integral constants of the outer voltage control loop. v_{err} represents voltage error. For achieving better DC bus voltage regulation by effective sharing of total current demand(i_{tot}). In conventional control scheme, LPF extracts steady-state part from total current (i_{tot}).

$$i_{B,ref}(s)=i_{std}(t)=\frac{w_c}{S+w_c}.i_{tot}(s), \tag{9}$$

where w_c represents LPF cut-off frequency and $i_{B,ref}(s)$ represents the battery current reference for the battery control loop. Steady-state current is controlled by battery system. Due to slow response of battery system, uncompensated power is observed from the battery system. The battery uncompensated power is given as follows.

$$P_{B\_un}(s) = \left(i_{B,ref}(s) - i_B(s)\right).V_B(s) \tag{10}$$

$$P_{B\_un}(s) = i_{B,err}(s).V_B(s), \tag{11}$$

where $P_{B\_un}(s)$ is the uncompensated power from the battery system. In the proposed control strategy, uncompensated power is utilized to improve the performance of the SC. Utilizing both uncompensated power and transient current component to design new SC reference current is given as follows.

$$i_{tran}(s) = \left(1 - \frac{w_c}{S + w_c}\right).i_{tot}(s) \tag{12}$$

$$i_{SC,ref}(s) = i_{tran}(s) + \left(i_{B,ref}(s) - i_B(s)\right).\frac{V_B(s)}{V_{SC}(s)}. \tag{13}$$

The battery and SC reference currents are compared with actual currents. Battery and SC error current are fed to PI controller. The duty cycle is calculated for the respective current references. d_B and d_{SC} are the duty cycle for battery control and SC control as shown in Figure 7A,B.

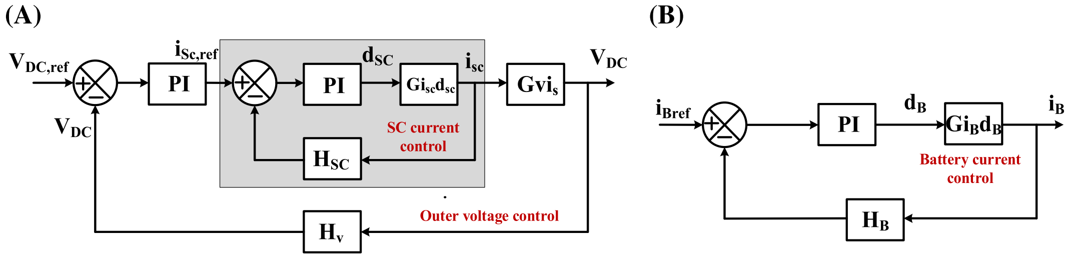

FIGURE 8 Block diagram representation A, supercapacitor control logic and B, battery control logic

TABLE 4 Small signal linear averaged transfer functions

Control to SC current transfer function
$G_{i_{SC}d_{SC}} = \frac{i_{SC}(s)}{d_{SC}(s)} = \frac{V_{DC}(1+d_{SC})}{R(1-d_{SC})^3}\left[\frac{1+S\frac{RC}{(1+d_{SC})}}{S^2-\frac{L_{SC}C}{(1-d_{SC})^2}+S\frac{L_{SC}}{R(1-d_{SC})^2+1}}\right]$
SC current to output voltage of transfer function
$G_{v_{DC}i_{SC}} = \frac{V_{DC}(s)}{i_{SC}(s)} = \frac{R(1-d_{SC})}{(1+d_{SC})}\left[\frac{1-S\frac{d^{L_{SC}}}{R(1-d_{SC})^2}}{1+S\frac{RC}{1+d_{SC}}}\right]$
Control to battery current transfer function
$G_{i_Bd_B} = \frac{i_B(s)}{d_B(s)} = \frac{V_{DC}}{d_BR(1-d_{SC})^2}\cdot\left[\frac{1+SRC}{S^2\frac{L^C}{(1-d_{SC})^2}+S\frac{L_B}{R(1-d_{SC})^2}+1}\right]$
PI controller transfer function of inner SC current loop
$G_{pi,SC} = K_{p.SC} + \frac{K_{i,SC}}{S}$
PI controller transfer function of battery current loop
$G_{pi,BAT} = K_{p,b} + \frac{K_{i,b}}{S}$
PI controller transfer function of outer voltage control loop
$G_{pi,v} = K_{p,v} + \frac{K_{i,v}}{S}$

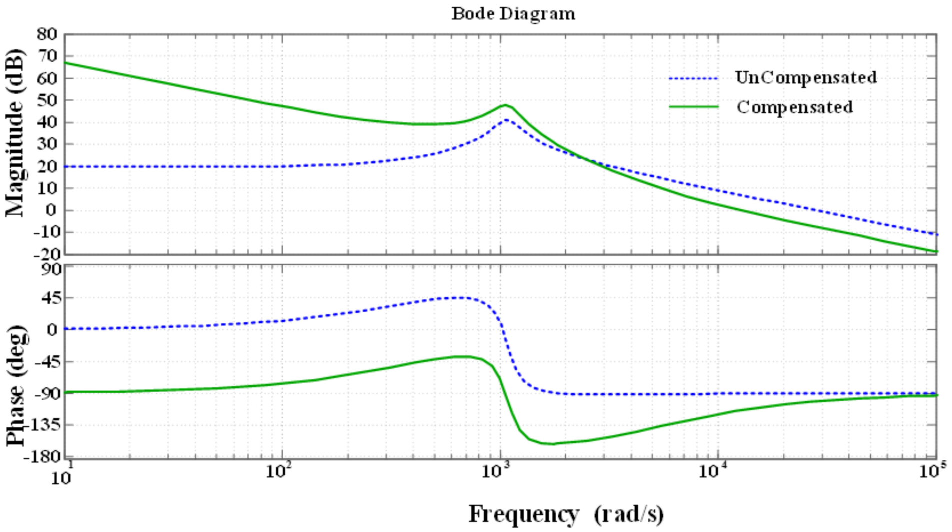

FIGURE 9 Bode plot of inner SC current logic for with and without compensation

4 | CONTROLLER DESIGN FOR HESS

The control system block diagram representation consists of an inner SC current loop and outer voltage loop as shown in Figure 8A. Similarly, battery current reference is regulated by using current control as shown in Figure 8B. SC current control loop bandwidth is higher compared to battery current control for the fast response. Inner SC current loop operates faster compared to outer voltage loop. Hence, current loop bandwidth is maintained more than voltage loop. Switching frequency is selected as 10 kHz in this work.

4.1 | Design of SC current control loop

The small signal transfer functions, calculated for the control parameters of SC control loop, are represented in Table 4. In Table 4, V_{DC} represents DC grid voltage, i_B: battery current, i_{SC}: SC current, d_B: duty cycle of battery current controller, and d_{SC}: duty cycle of SC current controller, respectively. The open loop transfer function $G_{i_{SC}d_{SC}}$ is used to determine current compensated parameters. In Table 4, $K_{p,SC}$ and $K_{i,SC}$ are the proportional and integral gains for the SC current controller. PI controller parameters for SC inner current control are obtained by selecting bandwidth of 1.6 kHz and phase margin of 60°. By using MATLAB SISO tool box, the SC current compensated parameters computed are $K_{p.SC} = 0.4124$ and $K_{i,SC} = 2291$.

The open loop and closed loop transfer functions for SC current control loop are determined for stability analysis of the system.

$$G_{ol\_SC} = G_{pi,sc}.G_{i_{SC}d_{SC}}.H_{SC}$$

$$G_{cl\_SC} = \frac{G_{pi,sc}.G_{i_{SC}d_{SC}}.}{1 + G_{pi,sc}.G_{i_{SC}d_{SC}}.H_{SC}},$$

where G_{ol_SC} represents open loop transfer function, G_{cl_SC} represents closed loop transfer function, and H_{SC} represents feedback gain of SC current control loop. The compensated and uncompensated bode plots for open loop SC current control loop are as shown in Figure 9. The bode plot representing designed controller is stable for a given phase margin and gain margin.

4.2 | Design of battery current control loop

The battery current control loop small signal transfer functions are given in Table 4. The open loop transfer function of battery control $G_{i_B d_B}$ is used to determine control gains. In Table 4, K_{p_b} and K_{i_b} represent proportional and integral gains for battery control loop. The battery controller gains are calculated using phase margin of 59.2° and bandwidth of 1 kHz. By using MATLAB SISO toolbox control parameters are calculated to be $k_{p\_b} = 1.971$ and $k_{i\_b} = 7300$.

$$G_{ol\_B} = G_{pi,B}.G_{i_B d_B}.H_B$$

$$G_{cl\_B} = \frac{G_{pi,B}.G_{i_B d_B}}{1 + G_{pi,B}.G_{i_B d_B}.H_B},$$

where G_{ol_B} represents open loop transfer function and H_B represents feedback gain for battery control loop. The compensated and uncompensated bode plots for open loop transfer functions are shown in Figure 10. Bode plot shows that designed control is stable for given phase margin and gain margin.

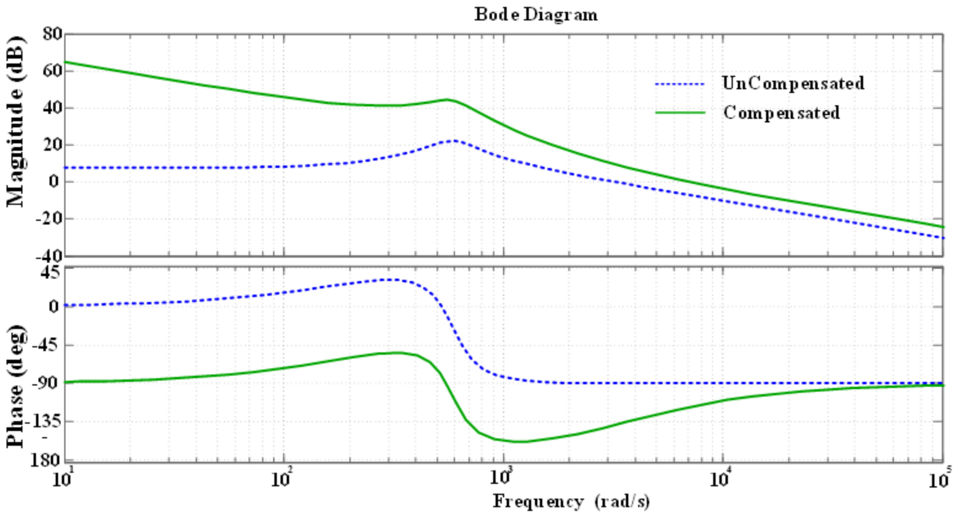

FIGURE 10 Open loop bode plot of battery current logic for with and without compensation

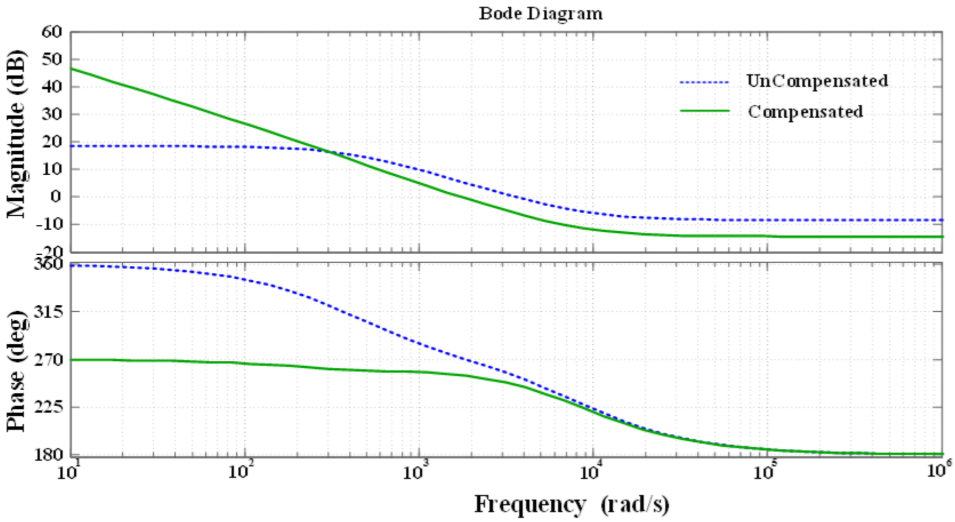

FIGURE 11 Open loop bode plot of outer voltage logic for with and without compensation

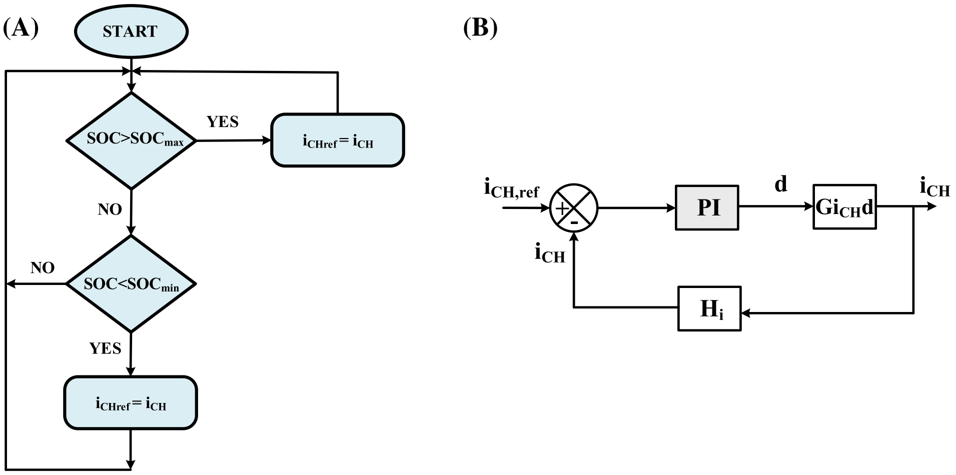

FIGURE 12 SOC charge controller for SC; A, logic to select between charging and discharging. B, control logic diagram

4.3 | Overall outer voltage control loop

Battery and SC current compensated values are required for design of voltage control loop. Bandwidth of 200 Hz and phase margin of 60° are selected for designing of outer voltage control loop. The proportional and integral gains for the outer voltage loop are obtained as $K_{p,v} = 0.5054$ and $K_{i,v} = 266$. Open loop transfer function of outer voltage control loop is calculated as follows.

$$G_{ol\_v_{DC}} = G_{pi,v}.G_{cl\_SC}.Gvi_{SC}.H_V.$$

Stability of the system calculated by using $G_{ol\_v_{DC}}$. Where H_V represents feedback gain of voltage control loop. The open loop transfer function of voltage control system for compensated and uncompensated bode plot is shown in Figure 11. For the required phase margin and gain margin, the bode plot shows that system is stable for the given operating point.

4.4 | Supercapacitor state-of-charge controller

Unlike batteries, supercapacitors have low ESR. So, they cannot retain energy for long duration. In order to prevent supercapacitor energy from getting depleted beyond a minimum permissible point, a control logic is designed to maintain the SOC within required limits. Whenever this desired range of SOC is violated, the converter enters into HESS energy exchange mode as explained in section II. When SOC of supercapacitor falls below prescribed minimum limit, it is charged with a constant current, I_{CH}, with battery power. When SOC exceeds the maximum safe limit, supercapacitor is allowed to discharge its excess energy to battery with a constant current, I_{CH}. Thus, SOC of supercapacitor is maintained within the limits by either buck (SC charging) or boost (SC discharging) operation as explained in section II.

The control logic for SOC controller is shown in Figure 12. A PI controller is used to regulate the supercapacitor current. The controller is designed based on buck mode control-to-output transfer function. Since its design is not within the scope, it is not shown here. Same controller is sufficient for buck and boost operation in HESS energy exchange mode explained above since transfer function is same for both the operations. It is to be noted that whenever HESS energy exchange mode is active, either due to low SOC or high SOC, dc microgrid is isolated from HESS electrically.

5 | SIMULATION STUDY AND DISCUSSION

In this segment, the results of the conventional and proposed control schemes are displayed for four test cases. The nominal parameters for simulation study are presented in Table 5. The entire model is implemented using MATLAB.

S. No	Parameters	Value
1	MPPT voltage (V_{mppt})	34.285 V
2	MPPT current (I_{mppt})	14 A
3	MPPT power (P_{mppt})	480 W
3	SC voltage (V_{SC})	32 V
4	SC inductance (L_S)	0.355 mH
5	Battery voltage (V_B)	24 V
6	Battery inductance (L_B)	0.3 mH
7	Boost inductance (L)	4.1 mH
8	Resistance (R)	4.8 Ω
9	DC grid voltage (V_{DC})	48 V
10	Capacitance (C)	300 μF

TABLE 5 Nominal parameters for simulation study

The model consists of two bidirectional converters—one for battery and other for SC. The PV array is a unidirectional, which is connected to the boost converter. The four operating cases are presented in the following sections for step change in PV generation and load demand.

5.1 | Case I: Step increase in PV generation

The simulation results for step change in PV generation, conventional and proposed control schemes are shown in Figure 13A,B, respectively. In both control schemes, due to atmospheric variations power produced by the PV panel increases from 480 W to 680 W at t = 0.4 s. Due to this PV current increases from 14A to 20A at t = 0.4 s. In this case load, power requirement is constant at 480 W. As PV power is more than the load power requirement, DC grid voltage increases more than 48 V. Immediately, SC absorbs excess power of 200 W in short duration until battery can regulate the grid voltage to 48 V. Thus, the battery and SC charge according to energy management scheme to maintain the grid voltage constant at 48 V. The simulation shows a settling time of 290 ms for conventional control scheme and 80 ms for proposed control scheme. The proposed control scheme has better dynamic performance and fast DC grid voltage regulation due to the utilization of uncompensated power from the battery system to improve the SC system.

5.2 | Case II: Step decrease in PV generation

The simulation results for step decrease in PV generation for conventional and proposed schemes are presented in Figure 13C,D, respectively. In both control schemes, due to atmospheric variations power produced by the PV panel changes from 680 W to 480 W at t = 0.4 s. The step decrease in PV generation causes step decrease in PV current from 20A to 14A. The sudden decrease in PV generation causes decrease in DC grid voltage. The settling time for conventional and proposed schemes is 220 and 60 ms, respectively. Proposed control scheme is approximately four times faster compared to conventional control scheme. From the results, it can be observed that performance of proposed scheme is better compared to conventional control scheme.

5.3 | Case III: Step increase in load demand

Simulation results for step increase in load demand for conventional and proposed control schemes are presented in Figure 14A,B, respectively. At an instant t = 0.4 second, load demand increases from 480 to 720 W. This increases the load current from 10 to 15 A. During this case, PV current is constant at 14A. Before t = 0.4 s, the steady-state values of V_{DC} = 48 V, i_{PV} = 14A, and i_o = 10A. At t = 04 s, the load demand increases to 720 W, which is beyond the power range of PV generation. This creates a power imbalance between source power and load power. Immediately, HESS responds, SC supply transient component of power demand and battery supplies steady-state component of power

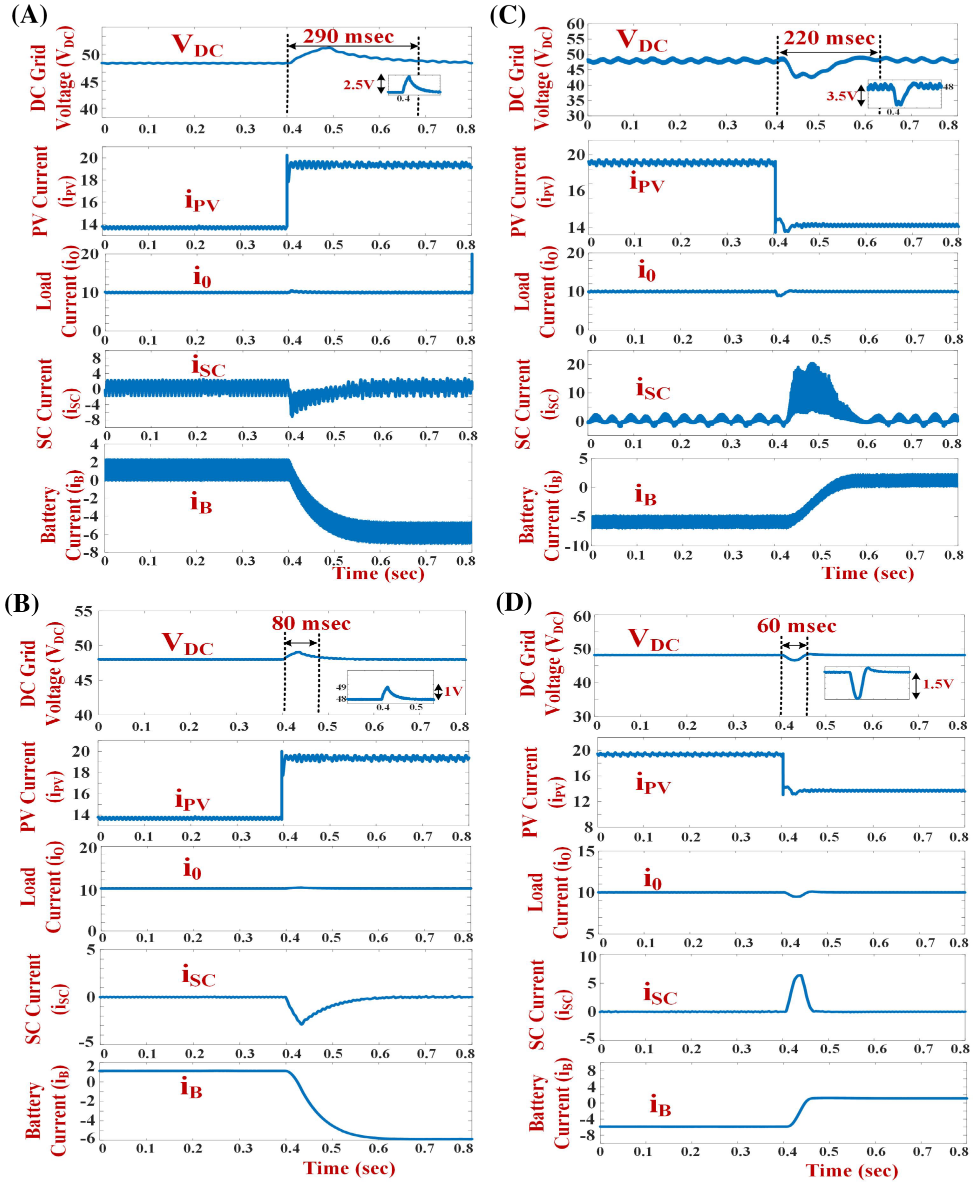

FIGURE 13 Simulation results for step increase in PV generation; A, conventional control scheme and B, proposed control scheme. Simulation results for step decrease in PV generation; C, conventional control scheme and D, proposed control scheme

demand. The DC grid voltage is regulated in 205 ms in conventional control scheme and 60 ms in proposed control scheme as shown in Figure 14A,B.

5.4 | Case IV: Step decrease in load demand

The simulation results for step decrease in load demand for conventional and proposed control schemes are presented in Figure 14C,D, respectively. At t = 0.4 s, load power demand decreases from 480 to 240 W. This causes load current changes from 10 to 5 A. The sudden change in load current affects the DC grid voltage. HESS responds immediately to these fluctuations to handle the excess power in the DC microgrid. The transient component of power handled is by the SC and average or steady-state component of power is handled by the battery in both the control schemes. The times taken to restore the voltage, in conventional and proposed control scheme, are 200 and 80 ms. From the results, it can be seen that the proposed control scheme is faster with less peak overshoot DC grid voltage compared to conventional control scheme.

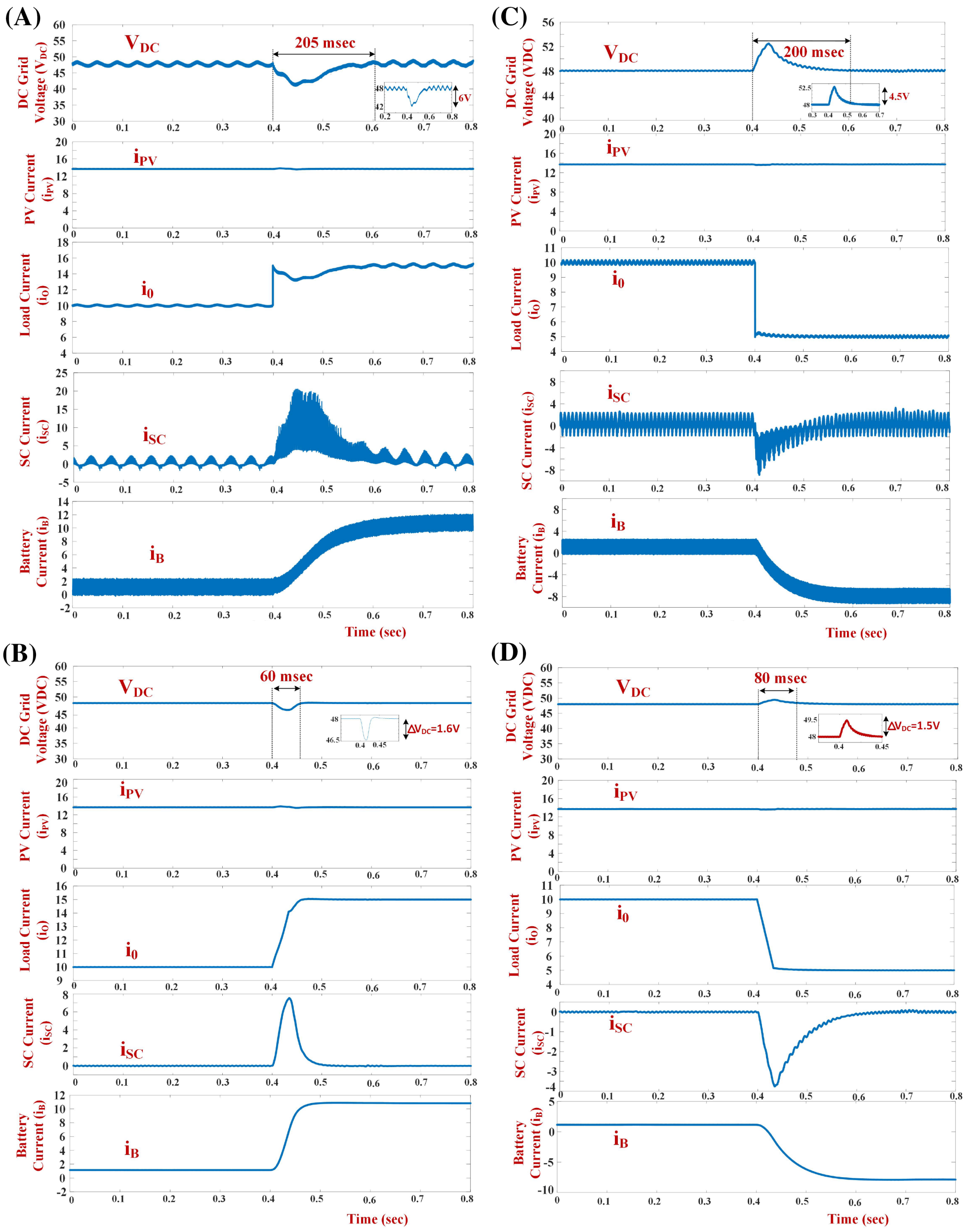

FIGURE 14 Simulation results for step increase in load demand; A, conventional and B, proposed. Simulation results for step decrease in load demand; C, conventional and D, proposed

5.5 | Comparative performance evaluation

The performance of the proposed control scheme is evaluated in comparison to the conventional control scheme with step change in PV generation as well as load demand for the peak overshoot and settling time to restore grid voltage. During step variation of PV generation and load demand, the maximum peak overshoot can be calculated as follows.

$$\%MP = \frac{\left|V_{DC,ref} - V_{max}\right|}{V_{DC,ref}} x100.$$

The comparative performance of conventional and proposed scheme is shown in Figure 15. It can be seen from the graphical representation that the proposed scheme is three times faster compared to conventional scheme. In the

FIGURE 15 Graphical comparative performance of proposed and conventional control scheme. A, settling time and B, peak overshoot

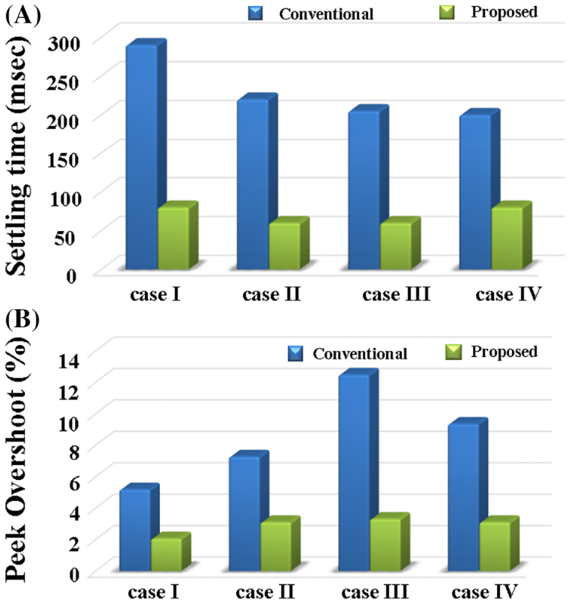

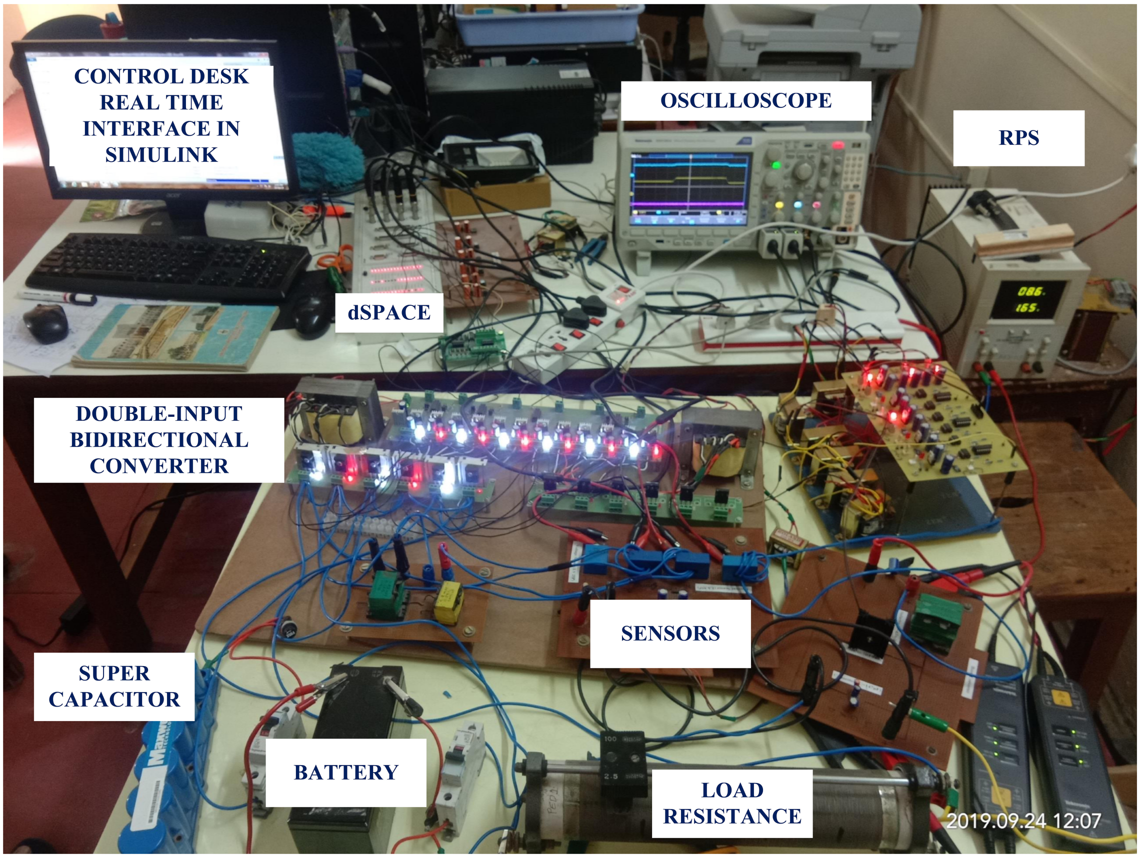

FIGURE 16 Hardware prototype developed for HESS

proposed control scheme, the maximum peak overshoot is also reduced in all four cases. Proposed control scheme is designed such that SC supports the HESS up to the time the battery reaches steady-state condition. The proposed scheme offers faster DC grid regulation with robust operation.

TABLE 6 DC microgrid implementation parameters

S. No	Parameters	Value
1	SC voltage (V_{SC})	10 V
2	SC inductance (L_S)	1.43 mH
3	Battery voltage (V_B)	12 V
4	Battery inductance (L_B)	4.8 mH
5	Boost inductance (L)	4.1 mH
6	Resistance (R)	25 Ω
7	DC grid voltage (V_{DC})	20 V
8	Capacitance (C)	150 μF

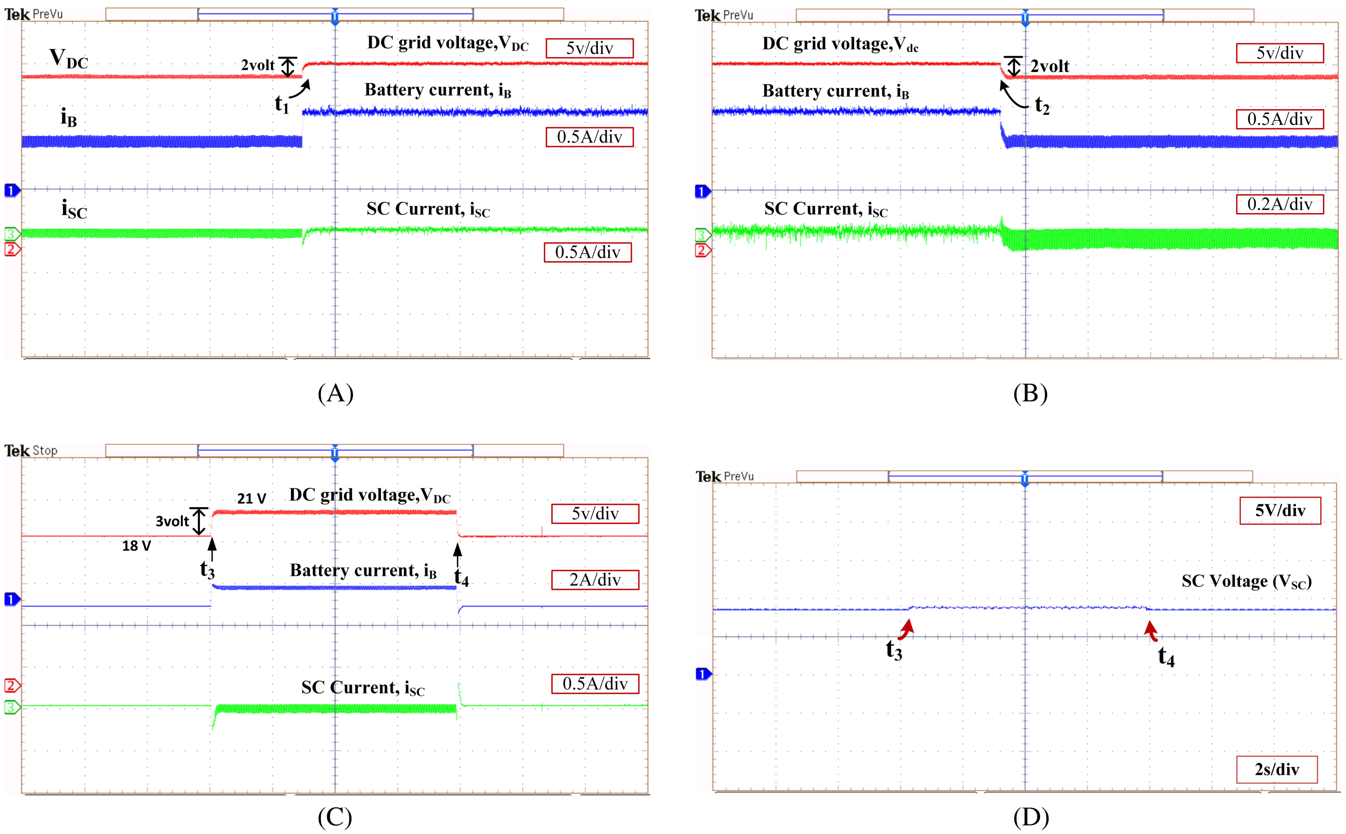

FIGURE 17 Experimental results for step variation in DC grid voltage reference; A, step increase in voltage reference, B, step decrease in voltage reference, C, step increase and decrease reference voltage, and D, SC voltage under step change in DC grid reference voltage

6 | EXPERIMENTAL RESULTS

The experimental setup developed for validation of a proposed controller for two-input bidirectional converter is shown in Figure 16. The dSPACE-DS1104 digital controller board is used in this work to generate switching pulses. The current sensor LA 55-P and voltage sensor LV 25-P are used for current and voltage measurements in the experimental validation. The regulated power supply (RPS) acts like PV emulator whose current is controlled by the boost converter. HESS is wired up using Exide Chloride 12 V, 7 Ah lead-acid battery and Maxwell BMOD0058 16 V, 58F supercapacitor. The bidirectional converter is connected using six MOSFET switches IRFP460.

The performance of DC microgrid supported by HESS is verified for different cases. (a) Step variation of DC grid reference voltage, (b) HESS charging mode, (c) HESS discharging mode, and (d) energy exchange mode. System implementation parameters for DC grid are given in Table 6. DC microgrid is designed at a nominal value of 20 V.

FIGURE 18 Hardware experimental results in HESS charging mode; A, DC grid voltage, battery current, and SC current, B, battery and SC SOC, and C, SC voltage waveforms

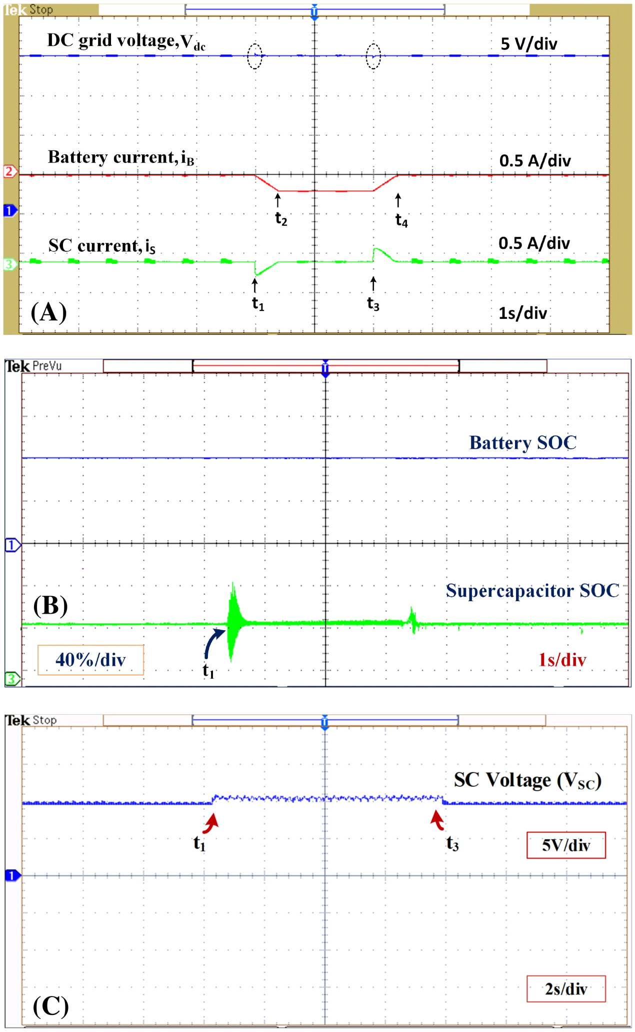

6.1 | Step variation of DC grid reference voltage

The experimental results for step change in DC grid voltage reference are shown in Figure 17. At time instant t_1, $V_{DC,ref}$ is step changed from 18 V to 20 V as shown in Figure 17A. In this case, load resistance and PV generation are kept constant at 25 Ω and 1.34 A, respectively. Smooth transition of DC grid voltage is observed. The HESS supplies required power to maintain the DC grid stability. SC supports transient current demand and battery supports steady-state demand to maintain the DC grid stability. Similarly, $V_{DC,ref}$ is step changed from 20 V to 18 V at time t_2 as shown in Figure 17B. Figure 17C,D shows the experimental results of step increase and decrease of DC grid reference ($V_{DC,ref}$). At time t_3, $V_{DC,ref}$ is changed from 18 to 21 V, and immediately, HESS supplies required power to maintain the DC grid stability. At time t_4, $V_{DC,ref}$ is changed from 21 V to 18 V, and immediately, HESS responds with transient component of current charging SC and steady-state component of current charging the battery to maintain DC grid voltage stability.

6.2 | Hybrid energy storage system charging mode

Here, performance of the designed controller in the scenario of surge in microgrid voltage either due to increased PV generation or due to decrease in load is analyzed. Waveforms are given in Figure 18. In this case, surge in microgrid voltage is realized by increasing load resistance. Initially, load resistance is R = 25 Ω up till the instant t_1. At t_1, load resistance is increased to 35 Ω, and, as a result, there is a decrease in load demand, and the excess energy in dc grid causes a surge in grid voltage. Immediately, HESS responds in such a manner that transient component of current is charging supercapacitor, and battery charging current is allowed to increase slowly till steady-state value at instant t_2.

At time instant t_3, load resistance is brought back to 25 Ω. The battery and SC currents are back to the original state as they were before time t_1. At time instant t_1 and t_3, the DC grid voltage almost constant at 20 V. Battery SOC, SC SOC, and SC voltage waveforms are shown in Figure 18B,C. At time instant t_1, SC SOC is increasing, indicating charging of SC. After the transient current period, SC remains idle as indicated by the constant SOC. Battery SOC is almost constant, its energy is not depleted as quickly, compared to the supercapacitor.

6.3 | Hybrid energy storage system discharging mode

In this case, performance of the controller is pitted against decrease in microgrid voltage either due to decrease in PV generation or due to increase in load. Waveforms are shown in Figure 19. Here, dip in microgrid voltage is realized by a decrease in PV generation. Decrease in PV generation is implemented by decreasing the input current (I_{PV}) of boost converter connected to RPS while maintaining input voltage (V_{PV}) constant at 12 V.

At time instant t_1, PV current decreases from 1.34 to 1.1 A. This causes power mismatch between source and load power, and there is a dip in the DC grid voltage. HESS supplies deficient power existing at the load side by discharging both battery and SC. The SC mitigates the transient power requirement and battery supplies steady-state requirement as shown by the current waveforms in Figure 19A. The combination of high-energy density battery and high power density SC maintains the DC grid voltage constant to the nominal value of 20 V. Due to fast dynamical performance, small spikes in DC grid voltage are negligible.

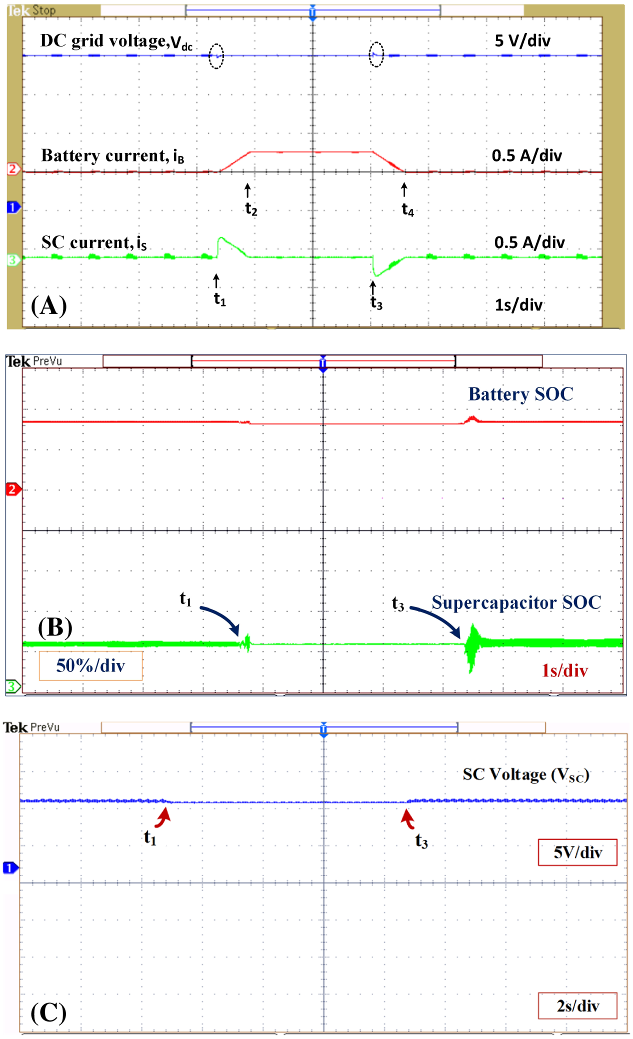

FIGURE 19 Hardware experimental results in HESS discharging mode; A, DC grid voltage, battery current, and SC current, B, battery and SC SOC, and C, SC voltage waveforms

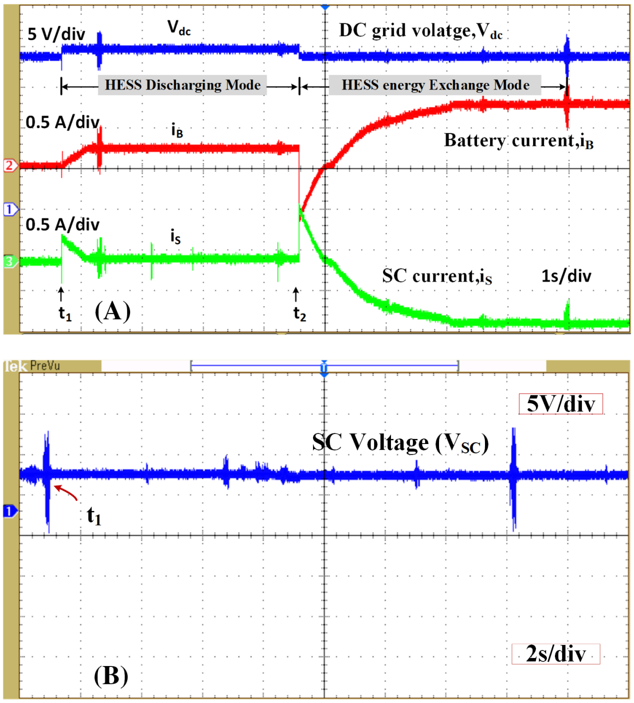

FIGURE 20 Experimental results for HESS energy exchange mode; A, DC microgrid voltage (V_{DC}), battery current (i_B), SC current (i_S). Transition from discharging mode to energy exchange mode. B, SC voltage waveforms

At time instant t_3, PV generation is brought back to normal state by making $I_{PV} = 1.34$ A. The SC current increases instantly, and battery current slowly reduces to zero, regulating DC grid voltage almost instantly. The battery SOC, SC SOC, and voltage waveforms are shown in Figure 19B,C validate the above explanation. At the instant t_1, due to decrease in PV generation, the SC SOC is found to be decreasing, indicating discharging operation of SC. After that period, the SC is idle as indicated by the constant SOC waveform. Similarly, at time instant t_3, SC SOC is increasing, indicating charging operation, and after that, it is idle.

6.4 | Energy exchange mode

The power flow from battery to SC is illustrated in this mode. Experimental results for energy exchange mode are shown in Figure 20A,B. Before time instant t_1, HESS is disconnected from DC microgrid, and in this period, grid voltage is 18 V due to reduced PV generation. At time instant t_1, HESS is connected for discharging of battery and SC to regulate DC grid voltage to 20 V. At time instant t_2, supercapacitor SOC is reduced to below 50%, which is taken as prescribed lower limit of SOC range, and then HESS shifts from discharging mode to energy exchange mode. Now, SC charges from the battery with a constant current of $i_{CH} = 0.8$ A. During energy exchange mode, HESS is disconnected from DC microgrid which is now evident from voltage waveform not being at the nominal voltage of 20 V.

7 | CONCLUSION

The performance of controller design, HESS modeling, converter design, and stabilization of DC microgrid against disturbances from PV generation as well as load variations is tested. The proposed system consists of PI controller, MIPC, DC sources and battery, and an SC based HESS. Battery current tracking error is observed in conventional control strategy. The error due to the battery current controller slows battery response. To address aforementioned issues, a proposed control strategy was developed, which provides fast DC grid voltage regulation compared with conventional control strategy. It utilizes battery error current to overcome slow dynamics of battery system. It decreases stress on battery and increases battery lifetime. Moreover, decoupled, separate, and independent control of battery and SC power was achieved as well as power flow between them. Low-power experimental setup is developed for two input bidirectional converter for step change in PV generation and load demand. This system can be applied in HEVs where more than two sources can supply power to the motor.

PEER REVIEW

The peer review history for this article is available at https://publons.com/publon/10.1002/2050-7038.12774.

DATA AVAILABILITY STATEMENT

The data that supports the findings of this study are available within the article and also in appropriate references.

ORCID

Srinivas Punna https://orcid.org/0000-0001-7074-1355
Arunkumar Chirayarukil Raveendran https://orcid.org/0000-0001-9426-5189

REFERENCES

1. Hredzak B, Agelidis VG, Jang M. A model predictive control system for a hybrid battery-ultracapacitor power source. *IEEE Trans Power Electron*. 2014;29:1469-1479.
2. Glavin M, Chan P, Armstrong S, Hurley W. A stand-alone photovoltaic supercapacitor battery hybrid energy storage systems. Paper presented at: 2008 13th International Power Electronics and Motion Control Conference; September 1-3, 2008; Poznan, Poland:1688-1695.
3. Hamzeh M, Ghazanfari A, Mohamed YAI, Karimi Y. Modeling and Design of an Oscillatory Current-Sharing Control Strategy in DC microgrids. *IEEE Trans Ind Electron*. 2015;62(11):6647-6657. https://doi.org/10.1109/TIE.2015.2435703.
4. Graditi G, Ippolito MG, Telaretti E, Zizzo G. An innovative conversion device to the grid Interface of combined RES-based generators and electric storage systems. *IEEE Trans Ind Electron*. 2015;62(4):2540-2550.
5. Choi ME, Kim SW, Seo SW. Energy management optimization in a battery/supercapacitor hybrid energy storage system. *IEEE Trans Smart Grid*. 2012;3(1):463-472.
6. Punna S, Manthati UB. Optimum design and analysis of a dynamic energy management scheme for HESS in renewable power generation applications. *SN Appl Sci*. 2020;2:495.
7. Laldin O, Moshirvaziri M, Trescases O. Predictive algorithm for optimizing power flow in hybrid ultracapacitor/battery storage systems for light electric vehicles. *IEEE Trans Power Electron*. 2013;28(8):3882-3895.
8. Chia YY, Lee LH, Shafiabady N, Isa D. A load predictive energy management system for supercapacitor-battery hybrid energy storage system in solar application using the Support Vector Machine. *Appl Energy*. 2015;137:588-602.
9. Song Z, Hofmann H, Li J, Hou J, Han X, Ouyang M. Energy management strategies comparison for electric vehicles with hybrid energy storage system. *Appl Energy*. 2014;134:321-331.
10. Torreglosa JP, Garcia P, Fernandez LM, Jurado F. Predictive control for the energy management of a fuel-cell–battery–supercapacitor tramway. *IEEE Trans Ind Inf*. 2014;10:276-285.
11. Bhomik P, Chandak S, Rout PK. State of charge and state of power management in a hybrid energy storage systems by the self-tuned dynamic exponent and the fuzzy-based dynamic PI controller. *Int Trans Electr Energy Syst*. 2019;29:e2848. https://doi.org/10.1002/2050-7038.2848.
12. Zhao C, Road SD, Kolar JW. An isolated three-port bidirectional DC-DC converter with decoupled power flow management. *IEEE Trans Power Electron*. 2008;23(5):2443-2453.
13. Zeng J, Qiao W, Qu L, Jiao Y. An isolated multiport DC–DC converter for simultaneous power management of multiple different renewable energy sources. *IEEE J Emerg Sel Top Power Electron*. 2014;2(1):70-78.
14. Wang Y, Han F, Yang L, Xu R, liu R. A three-port bidirectional multi-element resonant converter with decoupled power flow management for hybrid energy storage systems. *IEEE Access*. 2018;6:61331-61341. https://doi.org/10.1109/ACCESS.2018.2872683.
15. Yang P, Tse CK, Xu J, Zhou G. Synthesis and analysis of double-input single-output DC/DC converter. *IEEE Trans Ind Electron*. 2015;62(10):6284-6295.
16. Khaligh A, Cao J, Lee YJ. A multiple-input DC–DC converter topology. *IEEE Trans Power Electron*. 2009;24(3):862-868.
17. Wang B, Liang X, Manandhar U, et al. Hybrid energy storage system using bidirectional single-inductor multipleport converter with model predictive control in DC microgrids. *Electr Power Syst Res*. 2019;173:38-47.
18. Faraji R, Farzanehfard H. Soft-switching nonisolated high step-up three-port DC-DC converter for hybrid energy systems. *IEEE Trans Power Electron*. 2018;33(12):10101-10111. https://doi.org/10.1109/TPEL.2018.2791840.
19. Sato Y, Uno M, Nagata H. Nonisolated multiport converters based on integration of PWM converter and phase-shift-switched capacitor converter. *IEEE Trans Power Electron*. 2020;35(1):455-470. https://doi.org/10.1109/TPEL.2019.2912550.
20. Yi Z, Dong W, Etemadi AH. A unified control and power management scheme for PV-battery-based hybrid microgrids for both grid-connected and islanded modes. *IEEE Trans Smart Grid*. 2018;9(6):5975-5985.
21. Behjati H, Davoudi A. Power budgeting between diversified energy sources and loads using a multiple-input multiple-output DC-DC converter. *IEEE Trans Ind Appl*. 2013;49(6):2761-2772.
22. Filsoof K, Lehn PW. A bidirectional multiple-input multiple-output modular multilevel DC-DC converter and its control design. *IEEE Trans Power Electron*. 2016;31(4):2767-2779.
23. Wai RJ, Lin CY, Chen BH. High-efficiency DC-DC converter with two input power sources. *IEEE Trans Power Electron*. 2012;27(4):1862-1875.

24. Nejabatkhah F, Danyali S, Hosseini SH, Sabahi M, Niapour SM. Modeling and control of a new three-input DC–DC boost converter for hybrid PV/FC/battery power system. *IEEE Trans Power Electron*. 2012;27(5):2309-2324.
25. Wai RJ, Chen BH. High-efficiency dual-input interleaved DC-DC converter for reversible power sources. *IEEE Trans Power Electron*. 2014;29(6):2903-2921.
26. Chen CW, Liao CY, Chen KH, Chen YM. Modeling and controller design of a semiisolated multiinput converter for a hybrid PV/wind power charger system. *IEEE Trans Power Electron*. 2015;30(9):4843-4853.
27. Danyali S, Hosseini SH, Gharehpetian GB. New extendable single-stage multi-input DC–DC/AC boost converter. *IEEE Trans Power Electron*. 2014;29(2):775-788.
28. Guo F, Fu L, Zhang X, Yao C, Li H, Wang J. A family of quasi-switched-capacitor circuit-based dual-input DC/DC converters for photovoltaic systems integrated with battery energy storage. *IEEE Trans Power Electron*. 2016;31(12):8237-8246.
29. Gummi K, Ferdowsi M. Double-input DC-DC power electronic converters for electric-drive vehicles—Topology exploration and synthesis using a single-pole triple-throw switch. *IEEE Trans Ind Electron*. 2010;57(2):617-623.
30. Ahrabi RR, Ardi H, Elmi M, Ajami A. A novel step-up multiinput DC–DC converter for hybrid electric vehicles application. *IEEE Trans Power Electron*. 2017;32(5):3549-3561.
31. Akar F, Tavlasoglu Y, Ugur E, Vural B, Aksoy I. A bidirectional nonisolated multi-input DC–DC converter for hybrid energy storage systems in electric vehicles. *IEEE Trans. Veh. Technol.* 2016;65(10):7944-7955.
32. Nahavandi A, Hagh MT, Sharifian MBB, Danyali S. A nonisolated multiinput multioutput DC–DC boost converter for electric vehicle applications. *IEEE Trans Power Electron*. 2015;30(4):1818-1835.
33. Rezzak D, Boudjerda N. Management and control strategy of a hybrid energy source fuel cell/supercapacitor in electric vehicles. *Int Trans Electr Energy Syst*. 2016;27(6):e2308. https://doi.org/10.1002/etep.2308.
34. Babaei E, Saadatizadesh Z, Ranjbarizad V. A new non isolated bidirectional DC-DC converter with ripple-free input current at low-voltage side and high conversion ratio. *Int Trans Electr Energy Syst*. 2017;28:e2494. https://doi.org/10.1002/etep.2494.
35. Suresh K, Chellammal N, Bharatiraja C, Sanjeevikumar P, Blaabjerg F, Nielsen JBH. Cost-efficient nonisolated three-port DC-DC converter for EV/HEV applications with energy storage. *Int Trans Electr Energy Syst.* 2019;e12008. https://doi.org/10.1002/2050-7038.120088.
36. Hintz A, Prasanna UR, Rajashekara K. Novel modular multiple-input bidirectional DC–DC power converter (MIPC) for HEV/FCV application. *IEEE Trans Ind Electron*. 2015;62(5):3163-3172.
37. Zhou H, Bhattacharya T, Tran D, Siew TST, Khambadkone AM. Composite energy storage system involving battery and ultracapacitor with dynamic energy management in microgrid applications. *IEEE Trans Power Electron*. 2011;26(3):923-930.
38. Sathishkumar R, Kollimalla SK, Mishra MK. Dynamic energy management of microgrids using battery supercapacitor combined storage. Paper presented at: 2012 Annual IEEE India Conference (INDICON); December 7-9, 2012; Kochi, India: 1078-1083.
39. Erickson RW, Maksimovic D. *Fundamentals of Power Electronics*. Berlin, Germany: Springer; 2007.
40. Prasanth S, Manthati UB, Vishnu Sidharthan P, Punna S. Efficient interleaved buck converter driver for led applications. Paper presented at: 2019 IEEE International Conference on Sustainable Energy Technologies and Systems (ICSETS); February 26-March 1, 2019; Bhubaneswar, India:206-212. https://dx.doi.org/10.1109/ICSETS.2019.8744943.

How to cite this article: Punna S, Manthati UB, Chirayarukil Raveendran A. Modeling, analysis, and design of novel control scheme for two-input bidirectional DC-DC converter for HESS in DC microgrid applications. *Int Trans Electr Energ Syst*. 2021;31:e12774. https://doi.org/10.1002/2050-7038.12774